MEDICAL ROBOTS

Soft robotic manipulator for intraoperative MRI-guided transoral laser microsurgery

Ge Fang[1], Marco C. K. Chow[1], Justin D. L. Ho[1], Zhuoliang He[1], Kui Wang[1], T. C. Ng[2], James K. H. Tsoi[2], Po-Ling Chan[3], Hing-Chiu Chang[4,5], Danny Tat-Ming Chan[6], Yun-hui Liu[7], F. Christopher Holsinger[8], Jason Ying-Kuen Chan[3]*, Ka-Wai Kwok[1]*

Magnetic resonance (MR) imaging (MRI) provides compelling features for the guidance of interventional procedures, including high-contrast soft tissue imaging, detailed visualization of physiological changes, and thermometry. Laser-based tumor ablation stands to benefit greatly from MRI guidance because 3D resection margins alongside thermal distributions can be evaluated in real time to protect critical structures while ensuring adequate resection margins. However, few studies have investigated the use of projection-based lasers like those for transoral laser microsurgery, potentially because dexterous laser steering is required at the ablation site, raising substantial challenges in the confined MRI bore and its strong magnetic field. Here, we propose an MR-safe soft robotic system for MRI-guided transoral laser microsurgery. Owing to its miniature size (Ø12 × 100 mm), inherent compliance, and five degrees of freedom, the soft robot ensures zero electromagnetic interference with MRI and enables safe and dexterous operation within the confined oral and pharyngeal cavities. The laser manipulator is rapidly fabricated with hybrid soft and hard structures and is powered by microvolume (<0.004 milliter) fluid flow to enable laser steering with enhanced stiffness and lowered hysteresis. A learning-based controller accommodates the inherent nonlinear robot actuation, which was validated with laser path–following tests. Submillimeter laser steering accuracy was demonstrated with a mean error < 0.20 mm. MRI compatibility testing demonstrated zero observable image artifacts during robot operation. Ex vivo tissue ablation and a cadaveric head-and-neck trial were carried out under MRI, where we employed MR thermometry to monitor the tissue ablation margin and thermal diffusion intraoperatively.

INTRODUCTION

Head and neck cancer (HNC) is the seventh most common cancer in the world, causing more than 450,000 deaths every year (*1*). Because these cancers are located in regions associated with critical functions (e.g., respiration, phonation, and deglutition), traditional open surgery or adjuvant therapy often results in patient morbidity including dysphagia and dysphonia. Transoral surgery has become a dominant alternative by performing tumor resection through the mouth, primarily aiming at organ preservation (*2*). However, this approach can still be associated with considerable detriment to the patient due to the lack of specialized instrumentation to facilitate working in these confined spaces. Ablation technologies—such as electrosurgical-based, ultrasonic energy, argon beam coagulator, and radiofrequency energy—enable local energy delivery to targeted lesions inside the body (*3*) and thus allow localized and controlled ablation for minimally invasive surgery. Among them, in particular for smaller lesions, lasers can provide precise energy deposition and ablation margin, as well as effective hemostasis.

Transoral laser microsurgery (TLM) serves as an alternative by using a highly localized laser beam to enable precise tissue incision (*4*). Laser therapy has been used in the treatment of a variety of HNCs, with laser ablative therapy most commonly used in the treatment of glottic cancers. Laser ablation in glottic cancers with ultranarrow margins has been shown to be effective in preserving vocal function without the need for further adjuvant radiotherapy (*5*). This can be used even for bulky tumors that are early stage, with the advantage of minimal thermal spread to the surrounding normal tissue (*6*). Now, with the human papilloma virus–associated oropharyngeal cancer epidemic that is associated with improved outcomes and where narrower margins for resections are needed, the use of laser for resections has been shown to improve pain scores and to reduce hospital stay and time to oral feeding when compared with the use of traditional cautery (*7*). Previous oncological studies (*8*–*10*) have demonstrated TLM's notable performance in treating laryngeal tumors with minimal adverse influence of vocal cord function and reasonable functional voice outcomes. A carbon dioxide (CO_2) laser ($\lambda \approx 10.6$ μm) with high absorption rate in soft tissues is the most common laser source in TLM. The lasers are normally delivered and maneuvered through a set of external prisms and mirrors, which provides laser beam projection and steering at the surgical site. However, clinical success can only be achieved when the target area is perpendicularly exposed to the laser beam. This demand for "line of sight" limits its use for oropharyngeal and laryngeal tumors, which requires extreme positioning of patients to achieve adequate tumor exposure when the laser is delivered through rigid optical components. Lasers with shorter wavelength, e.g., thulium ($\lambda \approx 2013$ nm) and blue light ($\lambda \approx$ 445 nm) lasers, were introduced to meet this challenge. They can be coupled into flexible optical fiber to enhance access to surgical targets and achieve efficient tissue dissection and excellent hemostasis (*11*). Fiber optic lasers are already used in clinical practice (*12*–*14*).

[1]Department of Mechanical Engineering, University of Hong Kong, Hong Kong, China. [2]Faculty of Dentistry, University of Hong Kong, Hong Kong, China. [3]Department of Otorhinolaryngology, Head and Neck Surgery, Chinese University of Hong Kong, Hong Kong, China. [4]Department of Diagnostic Radiology, University of Hong Kong, Hong Kong, China. [5]Department of Biomedical Engineering, Chinese University of Hong Kong, Hong Kong, China. [6]Department of Surgery, Chinese University of Hong Kong, Hong Kong, China. [7]Department of Mechanical and Automation Engineering, Chinese University of Hong Kong, Hong Kong, China. [8]Division of Head and Neck Surgery, Stanford University, Stanford, CA, USA.
*Corresponding author. Email: jasonchan@ent.cuhk.edu.hk (J.Y.-K.C.); kwokkw@hku.hk (K.-W.K.)

However, the difficulties in manual manipulation of flexible optical fibers have motivated its incorporation with surgical robotics systems.

Currently, there is a single transoral surgical robotic platform that is approved by the U.S. Food and Drug Administration for transoral minimally invasive surgery (*da Vinci*, Intuitive Surgical Inc., USA) (*15*). An alternative hybrid approach using endolaparoscopic instruments and a robotic Flex camera (Medrobotics, USA) (*16*) has also been approved for clinical use for head and neck surgery. Two pilot studies (*15*, *17*) have evaluated the feasibility of combining transoral robotic surgery with flexible fiberoptic laser technology, demonstrating enhanced precision, fine-cutting margins, reduced postoperative pain, and increased operation safety. However, despite robot assistance, surgeons must still depend on their experience to approximate a safe "deep margin" while avoiding injury to crucial neurovascular or muscular structures. In normal surgical settings, such intraoperative (intra-op) evaluation can only be performed through time-consuming and costly pathologic laboratory procedures such as frozen section analysis (*18*). Although frozen section performed immediately after resection is the current gold-standard approach, margin assessment performed simultaneously and in real time as the surgeon treats the tumor would present a notable advance.

Magnetic resonance (MR) imaging (MRI) has gained prevalence as an intra-op image guidance modality because it can clearly contrast cancerous tissue as well as critical neurovascular structures. MRI can form high-resolution three-dimensional (3D) surgical roadmaps for preoperative planning, delineating early stage (T1/T2) carcinoma (*19*), whereas real-time MRI can readily visualize the physiological changes of tissue due to successful or incomplete laser cutting/ablation. The live visualization of fine changes in tissue temperature (<1°C) is made possible by MRI thermometry (*20*), which has been widely adopted for thermal dose monitoring in MRI-guided focused ultrasound procedures (*21*), radiofrequency ablation (*22*), and interstitial laser ablation (*23*). Closed-loop control has also been demonstrated by using MR thermometry feedback (*24*). Some examples of commercial laser therapy systems that use real-time MRI thermometry include the Tranberg System (Clinical Laserthermia Systems Americas Inc.) and the NeuroBlate System (Monteris Medical Inc.). Pairing anatomical and thermal imaging, MRI stands to be the unique modality that can provide accurate intra-op monitoring of ablation depth relative to the underlying critical tissue, as well as the extent of thermal diffusion, which could facilitate the modulation of laser delivery through different parameters, e.g., laser pulse width, distance, and power. With MRI guidance, 3D resection margins can be monitored and evaluated intraoperatively and in real time to protect critical structures while resecting adequate margins. This may eliminate the need for frozen section analysis, improving the surgical workflow, shortening operative time, and improving patient outcomes.

At present, robotic platforms that are able to leverage real-time intra-op MRI guidance together with continuous control of laser beam projection for tumor ablation are rare. Researchers have targeted procedures such as percutaneous ablation of liver cancer (*25*, *26*) and prostate cancer (*27*–*29*), alongside neurosurgical procedures (*30*, *31*). However, these systems are primarily designed for contact or needle-based ablation wherein the laser tip is inserted through a single-entry point in the skin and directly into target lesions where it remains stationary during the ablation process. Any positional adjustments are made between subsequent ablations. Robot designs based on concentric tubes have been introduced to provide laser probe targeting under MRI (*32*, *33*). Concentric tube manipulators generally require sophisticated actuation settings to generate both rotational and linear motion, which also have to be located close to the robot end effector to minimize losses in transmission. This creates difficulty in the design of compact robots and their actuator setups, particularly when the robot must be accommodated and operated inside the standard MRI head/body coil. This is made further challenging by the common use of piezoelectric-based motors, which should not be placed near the imaging site to prevent EM-artifact generation on images. This results in relatively heavy and large external actuation systems that may require mounting to the MRI table, affecting surgical workflow and patient access. Snake-like robots (*34*, *35*) face similar challenges with actuator compactness and are typically not MRI compatible. Microrobotic steering systems have been used for endoscopic laser surgery (*36*, *37*); however, these systems are also generally not MRI compatible. These factors mean that the current MRI-guided robotic systems are not equipped for controlling noncontact, projection-based lasers, particularly within constrained anatomy such as the oral and pharyngeal cavities.

Soft robotic manipulators have a unique combination of properties that are not typically seen in surgical robotics. Driven by pressurized fluids, they have the potential to address these challenges through high conformability, dexterity, and the ability to be MR-safe. Researchers have sought to apply soft robotics to several clinical applications such as colonoscopy (*38*, *39*) and keyhole surgery (*40*). In those studies, they leveraged the safety and conformability of soft and flexible actuators, where precision is a secondary goal. Few studies have reported intra-op MRI-guided robotic systems, particularly at miniature scales, while maintaining sufficient accuracy for treatment. Submillimeter-scale laser manipulation is required in TLM (*34*) while still ensuring the safety of delicate surrounding structures.

To this end, we proposed a fluid-driven soft robotic system that uses reinforced miniature soft actuators to provide precise laser delivery for TLM. A hydraulic actuation approach is taken for its intrinsic MR safety and ability to miniaturize the robot design by allocating the larger actuator systems to outside of the MRI room (*41*). When compared with pneumatic actuation (*42*), hydraulics does not suffer from the high compressibility of air, which can cause mechanical transmission delay and associated control inaccuracies. The system generates zero electromagnetic (EM) interference, allowing the introduction of intra-op MRI guidance to evaluate the laser/tissue interaction process, which plays an important role in balancing adequate tumor resection and function preservation. The soft robotic system is compact (Ø12 × 100 mm) and lightweight (~200 g), while providing five degrees of freedom (DoFs) motion under MRI. Integrating with a laser fiber, the robot enables flexible delivery and precise targeting of surgical lasers. A miniaturized laser manipulator is designed with optimized reinforcement to provide delicate laser beam steering (±26°) in a confined area. The manipulator is actuated through microvolume (<0.004 ml) fluidic inflation of elastomer chambers, which are regulated with a learning-based controller. A fiberscope is used to monitor the laser spot footprint and provide closed loop guidance for laser beam steering control. During laser ablation, MR thermal imaging can be conducted to evaluate the heat diffusion in tissue, thus offering real-time monitoring of the ablation margin. 3D MR scanning can be performed intraoperatively to enable in situ assessment of the ablation completeness. The key contributions of our work can be differentiated as follows:

1) Development of an MR-safe endoscopic robot system allowing flexible access to lesions in the confined oral and pharyngeal

cavities. The system provides a stable platform for laser beam delivery and navigation to the targeted lesions under MRI guidance. The robot is compact and lightweight, enabling mounting on the patient and operation with standard imaging coils under MRI.

2) Design of a reinforced miniature fluid-driven soft manipulator capable of delicate, precise, and repeatable laser spot steering on mucosa. The MR-safe hydraulic actuation enables simultaneous robot operation and MRI while ensuring minimal image artifacts.

3) Experimental validation of intra-op MRI-guided robotic laser ablation on ex vivo tissue and cadaveric oropharyngeal tissue. Intra-op MR thermometry was used to monitor the laser ablation process. A learning-based controller was used to enable accurate visual servoing of the laser spot along a path prescribed in situ on the camera view. The controller was tested via path-following experiments with various patterns, e.g., a symbol of a bat and zigzag filling, which demonstrated submillimeter accuracy in both tracking a boundary and filling an area.

RESULTS

The proposed soft robotic platform for MRI-guided TLM is shown in Fig. 1A, Movie 1, and movie S1. A soft robot integrated with a lens-pigtailed laser fiber enables safe endoscopic intervention through dental anchorage in the oral cavity and directs energy delivery to the lesion target deep to the larynx. Two segments of the soft robot, i.e., active bending section and distal laser manipulator, were used to offer, respectively, coarse robot navigation and fine laser beam pan-tilting (Fig. 1B). Each segment comprises three elastomeric chambers with volume varied by fluidic inflation/deflation to provide omnidirectional bending. Miniature spring reinforcement constraints (SRCs) were integrated into the laser manipulator to enable repeatable and accurate steering of laser beam even inside a protective outer shell (Fig. 1C and movie S2). Together with insertion, the robot provides five DoFs in manipulating the laser lens. Insertion/retraction is achieved by using a two-cylinder hydraulic actuator, which is coupled with a passive bending section to transfer rotational displacement to linear advancement. Both the soft chambers and cylinders are hydraulically driven via 10-m-long pipelines that are channeled through the MRI room waveguide and connected to robot consoles in the control room. The robotic scope is compact with a size of Ø12 × 100 mm and is lightweight at ~200 g, thus allowing noninvasive mounting to the patient with a custom-made dental guard (Fig. 1D). MR-based tracking markers can be assembled with the dental guard to offer positional localization under (real-time) MRI, thus registering the robot base with anatomical MRI coordinates and allowing the introduction of intra-op MRI guidance to monitor the laser ablation progress. Intra-op MRI can provide clinicians with enhanced perception of tissue incision width and depth (*43*), while providing the

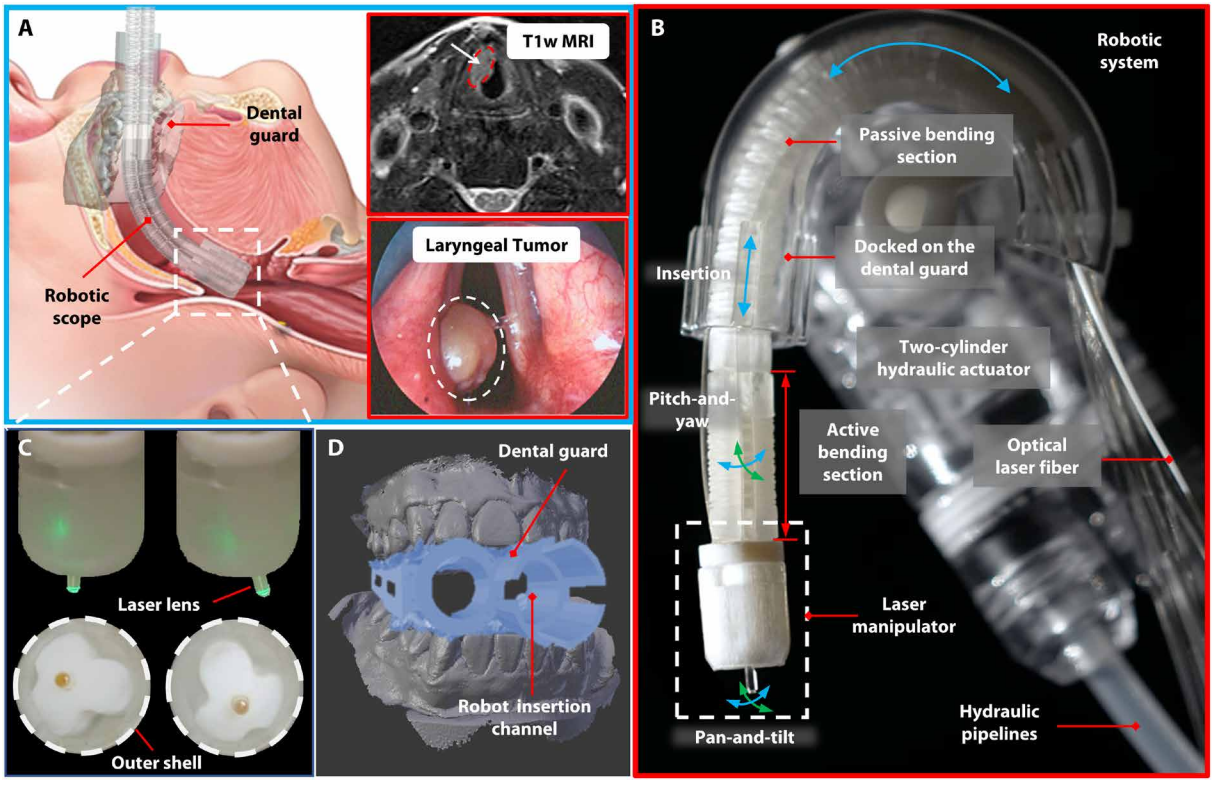

Fig. 1. Overview of the robotic system. (**A**) Illustration of the soft, fluid-driven robot positioned in the larynx through the oral cavity (left) and aiming at a laryngeal tumor (*60*, *61*) (bottom right). Intra-op MRI can be introduced to provide the operator with fine monitoring of the laser ablation progress (top right). (**B**) Overview of the five DoFs endoscopic motion. Pan and tilt are provided by both the active bending section and the laser manipulator. The passive bending section facilitates insertion and retraction of the robot by transferring rotation of the hydraulic actuator to linear motion. (**C**) Side view (top) and below view (bottom) of the soft laser manipulator, which enables omnidirectional laser beam steering inside a protective outer shell. (**D**) Patient-specific dental guard designed for robot anchorage and creating an open-jaw position of the patient.

unique capability of measuring dynamic changes of tissue temperature in 3D, which is crucial in alerting of excessive hyperthermia to the lesion surroundings, particularly in depth.

Soft robotic laser targeting system

To fulfill the rigorous requirement of MR safety, soft robots fabricated with elastomers, or polymer-based materials, are studied. These have gained increasing interest in medical applications, e.g., endoscopes, attributed to their flexibility and safe compliance with soft tissue surroundings. However, soft chambers made of pure elastomer material cannot sustain high pressure, limiting their loading capabilities and allowing uncontrolled expansion upon pressurization. Previous work proposed the restriction of soft chambers' radial expansion by paper-reinforced (*44*) or fiber-reinforced methods (*45*), which limited their deformation to 1D elongation. However, such reinforcement cannot improve the soft robots' stiffness, thus the mechanical responsiveness. The discrete constraint would also give rise to nonuniform distributions of the chamber wall thickness upon pressurization, which may result in high local stresses and rupture.

To this end, we proposed a soft robotic steering mechanism with an SRC to enable omnidirectional laser lens manipulation. The mechanism consists of three separate elastic chambers, located 120° apart in a triangular configuration. Reinforced springs fabricated from stiff materials were applied to the surface of each individual chamber during 3D printing. With the SRC, the soft chambers could bend with higher stiffness and lower hysteresis. The robotic scope is composed of two actuated segments. The distal segment, namely, the laser manipulator (Fig. 2A), incorporates SRC and soft chambers at a total length of 10 mm, offering omnidirectional pan/tilting of the laser lens in a local area (Fig. 2B). An extra outer shell (Ø12 mm) is designed to protect the laser beam maneuvering from external disturbances, e.g., contact with the oral and pharyngeal tissues. This isolation design enhances the robustness of laser manipulator and ensures laser beam steering with high accuracy. The second actuated segment, which is the active bending section (Fig. 2C), comprises three reinforced soft chambers in a total length of 24 mm and an outer diameter of 9.2 mm, providing coarse navigation for lesion

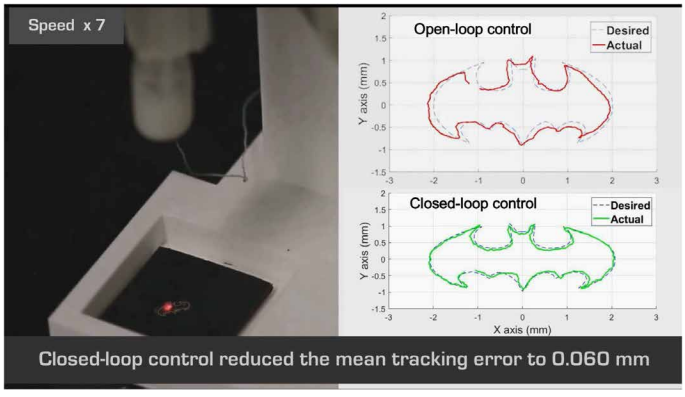

Movie 1. Overview of the proposed MRI-guided soft robotic system.

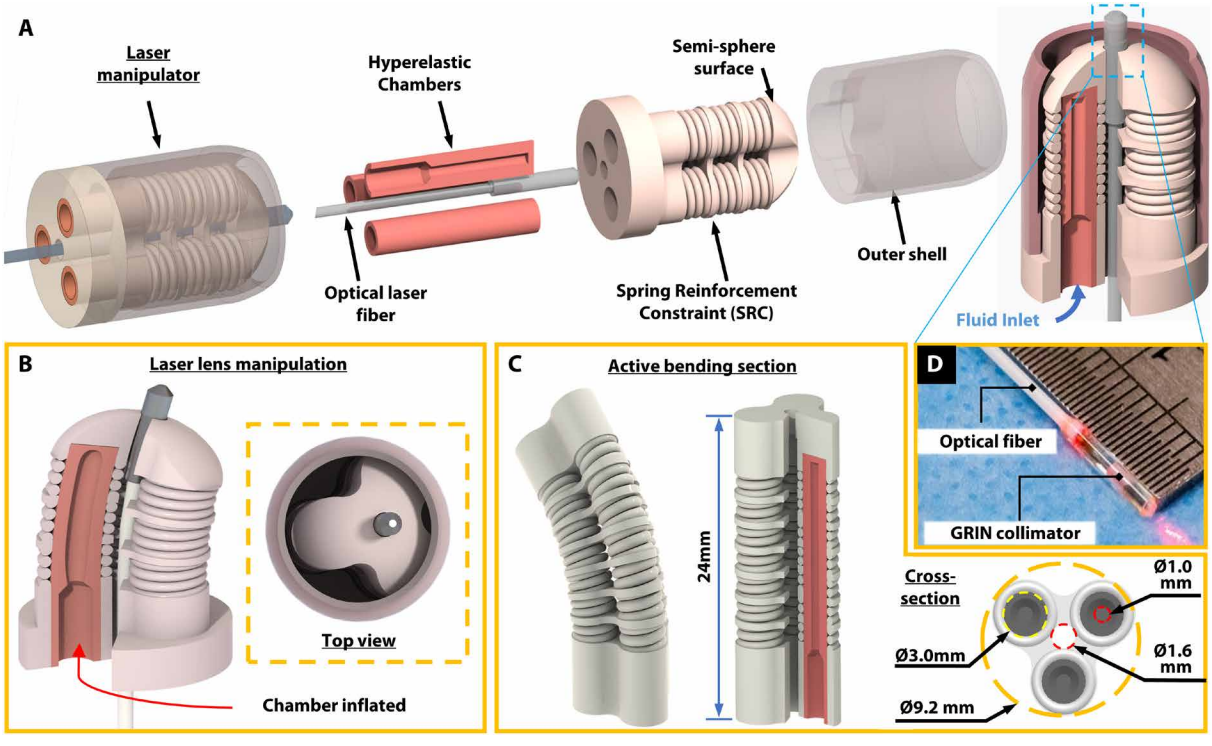

Fig. 2. Design of the soft robotic laser steering system. (**A**) Laser manipulator integrating three soft chambers with rigid SRCs. An outer shell protects the robot bending and laser steering from external disturbances. The hyperelastic chambers are 3D-printed from flexible AgilusClear30TM. The outer shell and SRCs are 3D-printed from VeroClearTM. (**B**) The laser lens is housed in the center channel of the laser manipulator and can be steered omnidirectionally. (**C**) Active bending section with a length of 24 mm and an outer diameter of 9.2 mm, comprising three soft chambers with individual spring constraints. (**D**) Gradient-index (GRIN) lens pigtailed with laser fiber.

targeting. The soft continuum segments were fabricated through 3D printing (Stratasys, Connex 3 Objet 350), which enables hybrid printing of rigid and soft materials. This fabrication method offers the option of fast robot customization, e.g., chamber lengths. There is a trend toward 3D printing materials that are biocompatible and sterilizable. However, the presented robot can also be fabricated by molding with mass-producible materials, e.g., medical-grade elastomers. In addition, the presented system is designed to be single use, which can reduce sterilization and cross-contamination concerns.

A fiberoptic medical laser enables flexible energy delivery toward target tumors located in the deep laryngeal region. An 808-nm diode laser with a power of 3 W was selected for our laboratory-based evaluation. The laser was guided by a 10-m-long optical fiber, with a core diameter of 105 μm. A green laser (532 nm) with a power of 10 mW was coupled into the same fiber to provide visual guidance. A gradient-index lens collimator (≈Ø1.2 × 9.0 mm) was assembled at the fiber tip to emit a parallel-beam spot on tissue (Fig. 2D). Compared with free-end fiber, the collimator could output a small laser spot (<1 mm) with high power density (>4 W/mm^2) even at long distance (~15 mm), hence allowing laser ablation without tissue-fiber contact. This minimizes the heat-affected zone on tissue and allows retention of the microlens after the procedure.

Docking and insertion mechanism

A docking mechanism was custom-made to provide stable robot mounting to patients in a noninvasive manner. A dental impression body was taken by using a fast-set dental alginate (Aroma Fine Plus) on the oral cavity and then casted with plaster. The cast was optically scanned to form the 3D dental feature. The tailor-made dental guard was constructed on the basis of the 3D cast with an open bite of 35 to 40 mm, allowing two entrances for endoscopic instruments to work in a workspace >40 mm by 40 mm by 20 mm. The workspace can be further enlarged by pressing the tongue downward using a plastic depressor, enabling the accommodation of more instruments guided by the endoscope. Several mechanical interlocks are featured on the dental guard to anchor the entire robotic mechanism. The robot can be securely mounted on the dental guard and allow docking through the oral cavity, thereby reducing the invasiveness to soft palate and uvula. Thin and tiny radio-frequency (RF) wireless resonators (*46*) (<Ø3 × 10 mm, capsulized with gadolinium-doped water) were fabricated and embedded inside the dental guard, providing high-contrast landmarks for registering the robot base in the MR image coordinates.

A rolling-diaphragm sealed hydraulic motor (*31*, *41*) was integrated to advance the bending sections. Linear hydraulic actuation was transmitted to rotary movement using a pair of pinion-and-rack units. Rolling diaphragms offers excellent sealing as well as negligible sliding friction. A curved channel was designed to guide the passive bending section of the robotic scope (Fig. 1B). A pair of semirigid 10-m-long pipes were used for the hydraulic transmission between MRI control room and scanner room. The liquid pressure was preloaded to 1 bar to reduce the backlash and enhance the transmission efficiency. The hydraulic motor provides a maximum linear stroke of 20 mm, driving each pinion by 100.6° and corresponding to a 50-mm robot insertion that is capable of reaching the oropharyngeal area. A concern related to the practical usage of hydraulic actuation under MRI is possible leakage or dripping when channeling the pipelines through the MRI waveguide. This problem can be addressed by incorporation of an automatic fluid circulation system, with which water can be automatically filled or drained as needed during setup.

Laser beam steering control

The active and passive bending sections of the robotic system are designed to guide the laser manipulator to the vicinity of the tumor region and provide an adequate angle for laser ablation. During the actual ablation process, only the distal laser manipulator is actively actuated and ultimately accounts for the overall laser steering precision of the system. To validate its accuracy, the laser manipulator was tested using a series of exercises that map to predefined patterns (movie S3). The laser manipulator was configured to scan the laser over an area of 15 mm by 15 mm on a projection plane located 15 mm below the robot tip, with a maximum bending angle of 26°. The scanning area is sufficient for coverage of an average oral tumor, which has been reported to have a mean length of 4.04 mm and a width of 3.08 mm when identified under MRI (*47*). Precise steering of the laser spot within a small and local area using the hydraulic-driven soft laser manipulator could raise challenges due to the actuation nonlinearity and fabrication uncertainty. To this end, a learning-based modeling method was implemented to characterize the robot kinematics, which establishes the mapping from laser spot movements on the projection plane to robot actuation. The laser spot position can be computed from robot tip orientation, which was measured using an EM-tracking system (Fig. 3A) or by directly extracting from camera images (Fig. 3B). On the basis of the trained model, a feed-forward controller was constructed to predict the actuation commands of three chambers for the desired laser spot positions. Four different path-following tests were performed under different laser control conditions. Open-loop laser spot tracking was used to follow spiral and pentagon paths with mean tracking errors of 150 and 189.4 μm, respectively (Fig. 3C). In the open-loop path following of the pentagon, we also calculated the repeatability of laser beam manipulation, which is measured as the deviation of successive cycles from the first cycle. The tracking results of pentagon path following demonstrated a mean deviation error of 44.6 ± 8.2 μm, which suggests that the robotic laser manipulator paired with the learning-based model could produce repeatable and accurate path following even with open-loop control.

To further improve the control accuracy, a closed-loop controller was also investigated. For the purpose of laboratory-based validation, we incorporated the EM tracker as feedback. The robot achieved enhanced tracking accuracy even when following an irregular path (i.e., symbol of a bat) with the root-mean-square tracking error reduced to 121.5 μm. Considering the limitation of EM sensors under MRI, we also investigated closed-loop visual servo control based on the MR-compatible fiberscope view. Apart from providing feedback for control, the fiberscope could view the laser spot projected on the surgical site, thus offering an interface for both task definition and visual monitoring. A 10-m-long fiber optic camera (Fig. 3B) was used to meet the requirements of operation under MRI. As demonstrated in Fig. 3D and movie S4, the laser spot could be accurately controlled to follow a four-leaf path defined in the camera view, with a mean tracking error of 1.04 pixels, corresponding to 69.3 μm on the projection plane. In ablation procedures, the laser spot footprint may need to fill a targeted area. Apart from the spiral pattern shown in Fig. 3C, the laser manipulator also maintained excellent accuracy when filling an area with complex boundary in zigzag pattern, as shown in fig. S1 and movie S5.

The tracking error statistics of the path-following experiments are shown in Fig. 3D, indicating that the laser manipulator is capable of tracing any basic and complex paths with high accuracy (<200 μm),

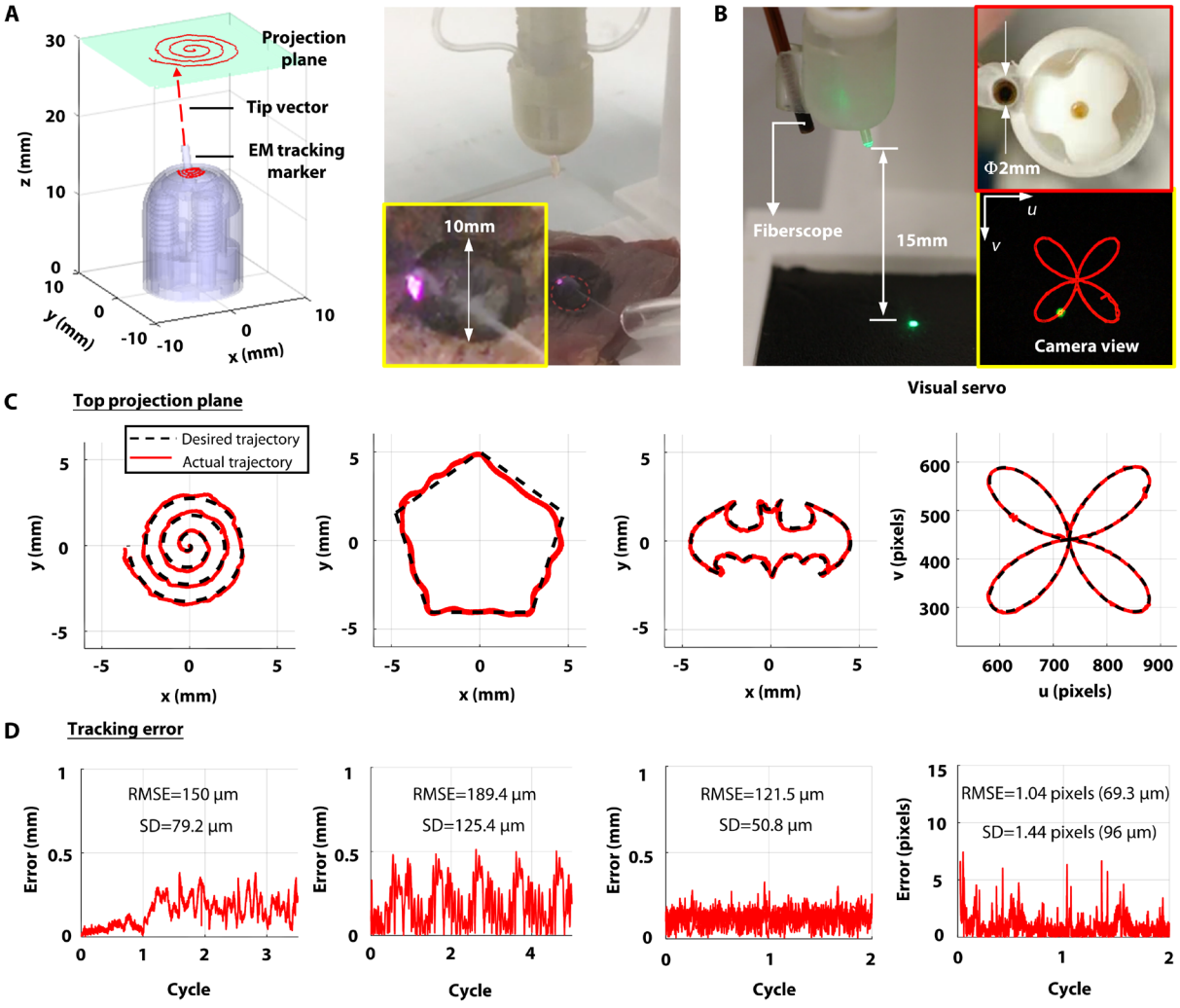

Fig. 3. Laboratory-based laser beam steering control. (**A**) Path following of the laser spot on a projection plane using the soft laser manipulator. The laser spot position can be determined on the basis of the robot tip position and orientation measured with an EM tracking system. (**B**) Laser spot visual servoing is achieved with an MRI-compatible fiberscope. (**C**) Laser spot trajectories tracked with open-loop control (columns 1 and 2), EM-tracked closed-loop control (column 3), and laser spot visual servoing control (column 4). (**D**) Associated tracking errors.

which meets the clinical requirements on laser spot targeting (<1 mm) (*34*). The spiral and pentagon pattern results demonstrate that the laser manipulator can accurately perform circular and linear motion that commonly comprises other, more complex patterns. In addition, the robot maintains high accuracy even on following complicated trajectories (e.g., a symbol of a bat) that involve sharp turns and thus sudden changes of the robot trajectory. This is typically a challenging task for soft robots to perform precisely due to the need for sudden volume changes of the robot's soft actuation chambers, coupled with the compliance of the robot body.

MRI compatibility

We evaluated MRI compatibility of the entire robot system with a 1.5-T MRI scanner (SIGNA HDxt, GE Healthcare) (Fig. 4A). The robot was placed beside a rectangular water phantom and translated to the isocenter of the scanner. As suggested in the American Society for Testing Materials (ASTM) F2119 standard, T1-weighted gradient echo (GRE) and T2-weighted fast spin echo (FSE) sequences were both implemented for image acquisition and comparison. A control image of the phantom alone was acquired as the baseline. After positioning the robot next to the phantom, MR images were obtained under three different robot conditions: (i) static: robot is powered off; (ii) powered: robot is at rest, but the hydraulic and electric power are on; and (iii) operating: robot is being actuated. The signal-to-noise ratios (SNRs) in MR images were calculated following the guidelines (*48*) by the National Electrical Manufacturer's Association. SNR losses compared with the control image were calculated over five image slices, which cover most of the water phantom. The mean SNR variation in T1-GRE and T2-FSE images with robot operated are 0.18 and −2.29%, respectively. An SNR loss up to 10% is suggested to be acceptable (*49*). The SNR loss compared with the control image is within 5% even with the robot in full motion, as shown in Fig. 4B. Image intensity variations of 30% or above were considered as artifacts referring to the ASTM standard test method (*50*) and would appear as white

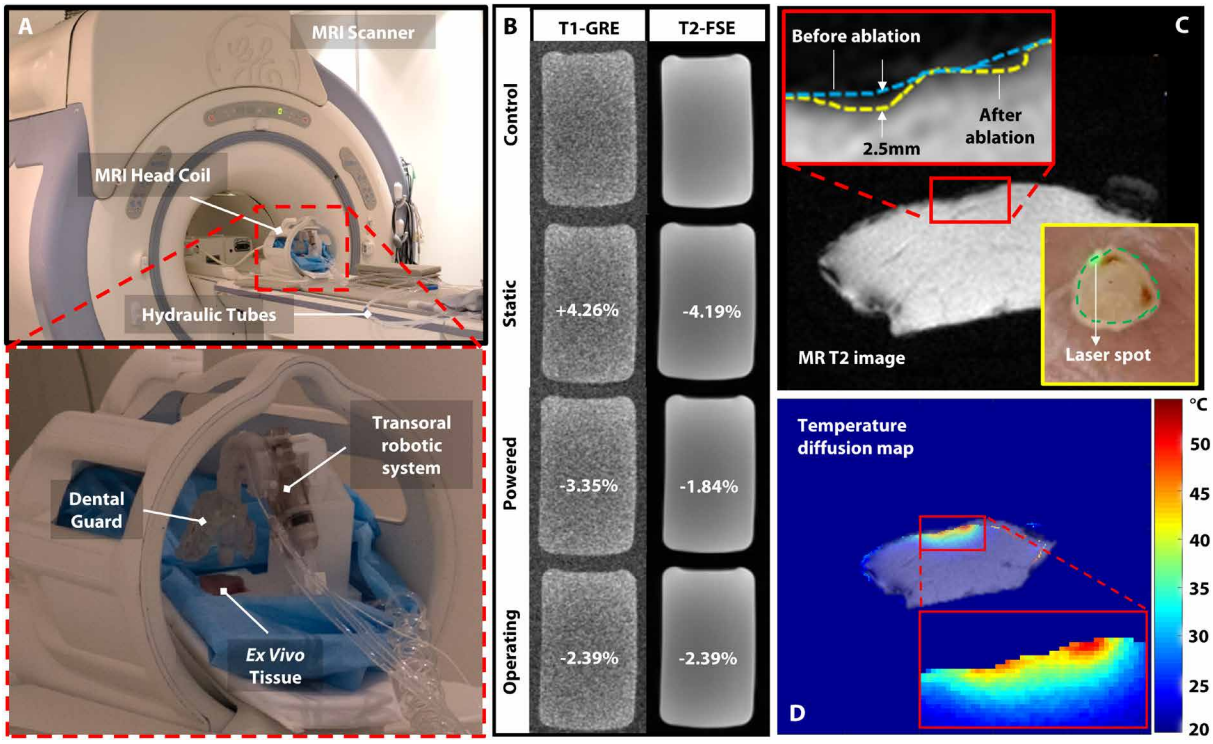

Fig. 4. MRI-based ex vivo laser ablation test. (**A**) Robot setup in the MRI scanner, with an eight-channel transmit/receive head coil for image acquisition. (**B**) MR images of a water phantom placed beside the robot, showing the normalized SNR loss during different states of robot operation. The robot is not present in the control case. (**C**) Observable ablation depth found in MR T2 images of swine tissue before and after ablation, with the laser spot controlled to follow a near-circular path. (**D**) MR thermometry applied to monitor thermal diffusion and accumulated temperature increments in tissue due to laser ablation.

pixels in the binary map. No observable image artifacts were found within the phantom area, which indicates that the robot operation at the isocenter generates zero EM interference to tissue imaging.

Ex vivo trial

To evaluate the feasibility of our soft robot telemanipulation, laser beam steering, and its intra-op MRI settings, ex vivo laser ablation test was conducted to monitor laser-induced changes on tissue. A head coil was used to house the robot and acquire MR images (Fig. 4A). The robot was remotely controlled to aim the laser spot along a near-circular trajectory. A continuous-wave laser source (1550 nm, 3 W) with a high absorption rate in water was used. A green laser with a wavelength of 520 nm was also combined into the ablation laser beam to offer visual indication of the ablation laser location using an MR-compatible fiberscope. A GRE sequence with parameters repetition time (TR)/echo time (TE) = 45/13.8 ms, flip angle = 12°, slice thickness = 8 mm, number of slices = 1, pixel size = 0.625 mm by 0.625 mm, and field of view = 160 mm by 160 mm was implemented to acquire both a magnitude and phase image at a time resolution of 10 s. This could be further accelerated by introducing advanced pulse sequences (*51*). The magnitude image directly gives the update of tissue morphology during the laser ablation. As shown in Fig. 4C, the laser ablation depth can be clearly seen and measured (~2.5 mm) from the MR images. On the basis of the phase images, the temperature increments relative to the baseline acquired before ablation could be calculated using the proton resonance frequency shift method (*52*). The accumulated thermal diffusion on this cross-sectional slice overlaid on the anatomical tissue image is shown in Fig. 4D, with the laser spot region generating the highest temperature increase. To cause irreversible cell death, the tissue must be heated to >42°C (*53*). Thermal dosage to the tissue can be monitored accordingly, which could offer a useful guidance to surgeons when controlling the laser projection and intensity. With advanced MRI sequences, multislice images can be taken in parallel (*54*) or orthogonally (*55*), thus providing 3D monitoring of the tissue thermal effect during laser ablation.

Cadaver trial

To validate the proposed robotic platform in human anatomy, we performed a cadaver trial of transoral laser ablation under a 3-T MRI scanner (Philips Achieva) (movie S6). The experimental setup is shown in Fig. 5 (A and B). A cadaver head was defrosted 24 hours before the test and fixed in an acrylic tube mount using plastic screws (Fig. 5C). The dental guard with an open bite of 35 mm was fitted in the mouth to create an open-jaw cavity. In addition, the tongue was retracted anteriorly with a 2-0 silk suture, and an L-shaped, 3D-printed depressor (90 mm by 20 mm by 2 mm) was used to push down the tongue and further increase the workspace. The depressor was tightened to the head fixture using fabric strings. The robot was then mounted on the dental guard and fixed through mechanical interlocks. A 10-m-long MR-compatible fiberscope, with an additional lighting fiber for illumination, provided the endoscopic view for simple navigation.

Three MR fiducial markers fabricated from capsulized gadolinium-doped water (concentration: 10 mM) were integrated with the dental guard to localize the robot base in MRI coordinates (Fig. 5D).

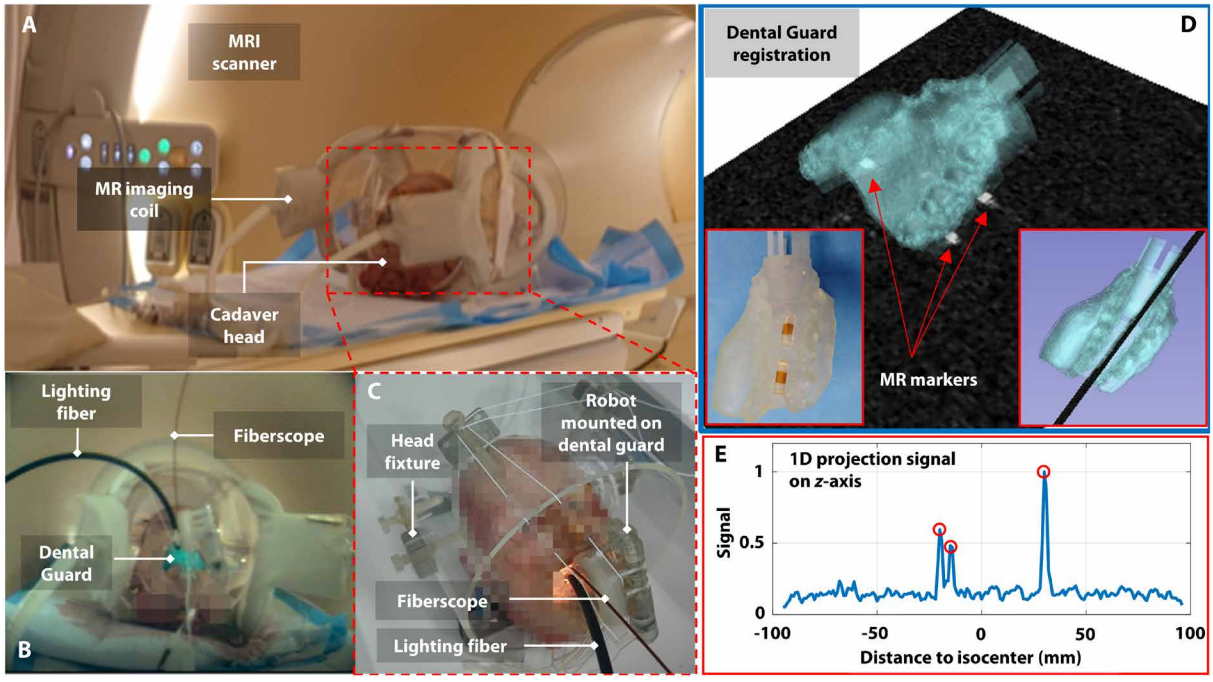

Fig. 5. MRI-based cadaver trial setup and registration. (**A**) Experimental setup in the 3-T MRI scanner (Philips Achieva). (**B**) Image acquired by an MRI-compatible camera, with the robot moved to the isocenter. (**C**) Cadaveric head fixed in an acrylic tube mount. A fiberscope and lighting guide were inserted through the additional channel of the dental guard. (**D**) Dental guard registered based on scanned MR tracking markers. (**E**) Corresponding *z*-axis 1D projection scan for localizing the three MR tracking markers.

Specifically designed miniature wireless MR resonators (*46*) were integrated into the fiducial markers to locally amplify their signal, providing high SNR even under low flip angle excitation (1°). The resonators are flexible printed LC circuits tuned to the Larmor frequency (63.87 MHz). The fiducial markers show high contrast in anatomical MR images, thus enabling positional localization. On the basis of the preoperative 3D imaging, positions of the markers can be identified from the anatomical background. With 3D positions of three markers inside the dental guard, point-based rigid registration can be performed to locate the dental guard and the robot base in MR image coordinates. Alternatively, using 1D-projection gradient readouts, the marker positions could even be obtained in real time (~30 Hz) (Fig. 5E). For preoperative planning, a T1-weighted imaging model of the head and neck region was acquired, using 3D GRE pulse sequence with the following parameters: TR/TE = 7.7/3.6 ms, slice thickness = 1.1 mm, flip angle = 8°, number of slices = 280, pixel size = 1.03 mm by 1.03 mm, field of view = 230 mm by 230 mm. The intra-op scanning plane for temperature measurement was determined on the basis of the reconstructed 3D head volume (Fig. 6A). The robot was positioned in the oral cavity of the cadaver, and a laser ablation trajectory was defined by the operator by "sketching" in the fiberscope camera view (Fig. 6B). Low-temperature laser visualized by MR thermometry could be applied to ensure that the ablation location is consistent to the preoperative plan made in the T2-weighted model. Control of the laser spot on the mucosa along the prescribed trajectory was achieved through machine learning–based visual servoing. Accurate laser spot steering was achieved with a mean tracking error of <3 pixels (~0.2 mm). The tracking performance of the first two ablation cycles is shown in Fig. 6C.

Once the lesion region was confirmed in the MR coordinates, the ablation laser was turned on and steered along the trajectory over multiple cycles (~35 s each) for 3 min, with a power of 3 W. Meanwhile, anatomical and temperature interleaved imaging was performed using a routine 2D FSE sequence with the following parameters: TR/TE = 15/5 ms, slice thickness = 2 mm, number of slices = 14, flip angle = 18°, pixel size = 0.479 mm by 0.479 mm, field of view = 230 mm by 230 mm, at a time resolution of 20 s. The update rate can be accelerated to even subseconds by tuning the sequence parameters, e.g., reducing the field of view and number of slices. As shown in Fig. 6D, a map of temperature increments can be obtained to reflect the thermal effect on tissue upon laser energy absorption. A postablation image was taken with a handheld camera (Fig. 6E), which showed an ablation pattern with similar boundary to the predefined trajectory. Coagulation occurred in the center due to the hyperthermia inefficiencies of the laser source, which could not produce rapid tissue vaporization. Optical fiber–guided thulium laser would be an alternative that can provide improved cutting and ablation properties comparable to that of the widely used CO_2 laser.

DISCUSSION

This paper presents the design and experimental validation of a soft robotic system for intra-op MRI-guided TLM. The robot comprises two actively steerable soft continuum segments that are driven by microvolume liquid flow (<0.004 ml) to the internal elastomer chambers, which are individually integrated with SRCs. The spring reinforcements were designed and optimized through finite element analysis (FEA) to balance between robot bending stiffness and maximum

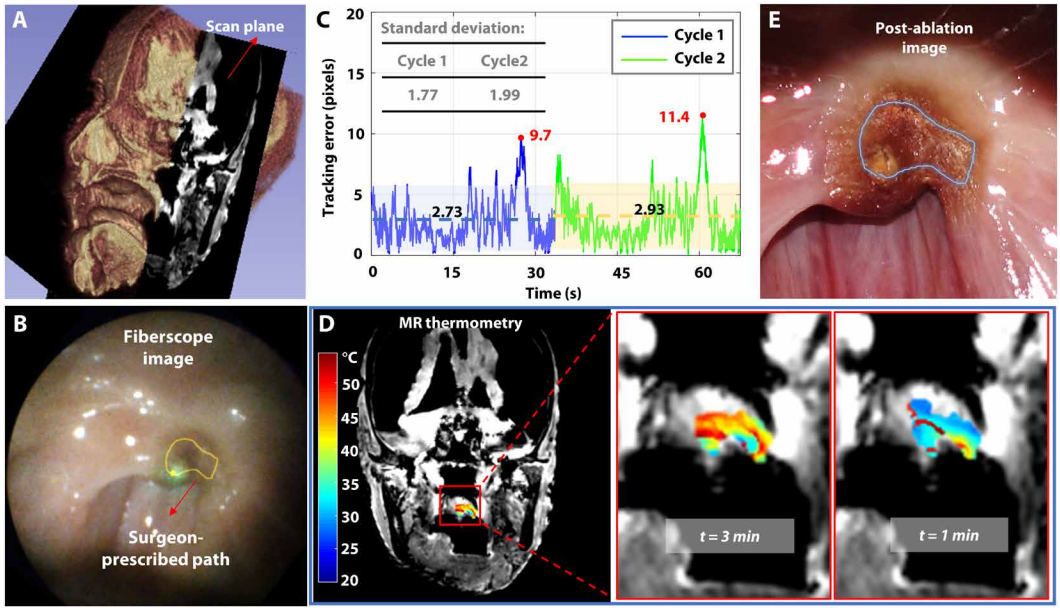

Fig. 6. MRI-based cadaver trial ablation result and MR thermometry. (**A**) Imaging slice prescribed for intra-op MR thermometry superimposed on the cadaver preoperative 3D model. (**B**) Laser spot controlled to follow a trajectory defined in the fiberscope view. (**C**) Tracking errors of laser spot path after over two initial cycles. (**D**) Temperature increment map overlaid on the anatomical MR image after 1 and 3 min of ablation. (**E**) Postablation image of the tissue.

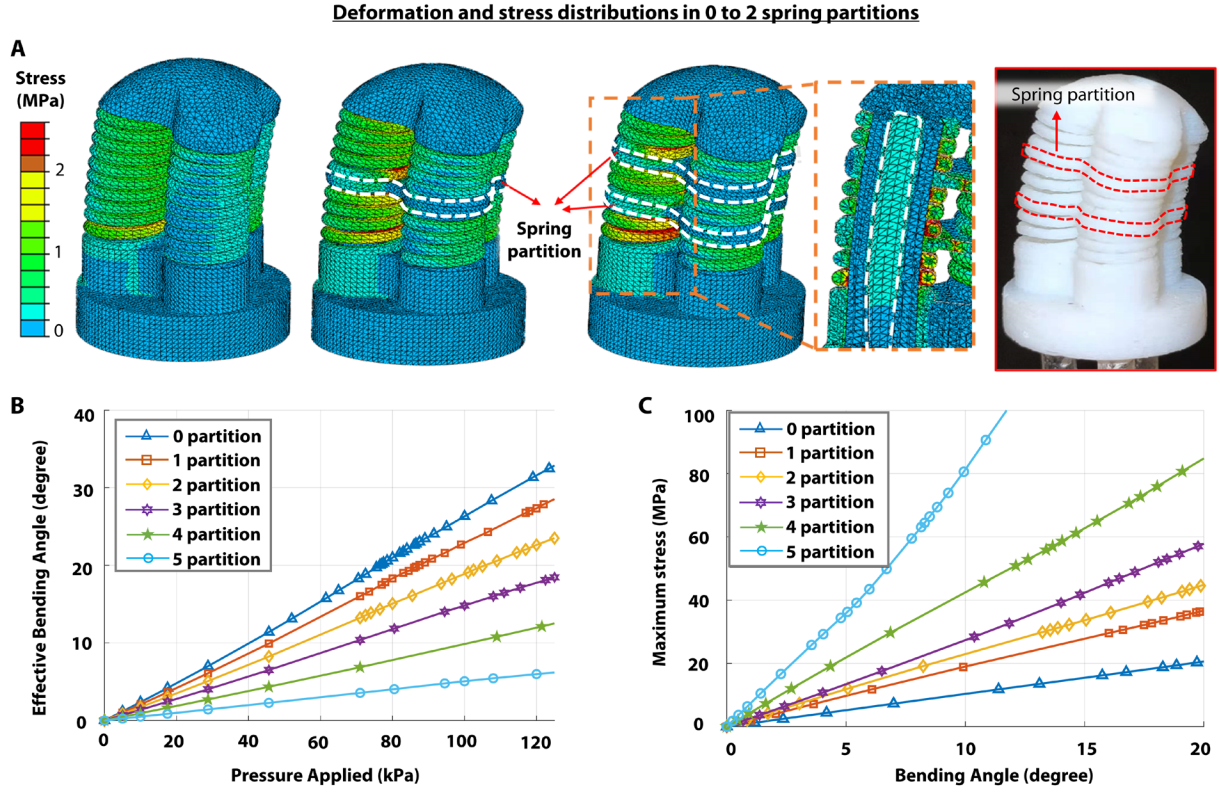

Fig. 7. Design optimization of the SRC. (**A**) Finite element–simulated deformation of the laser manipulator at a bending angle of 10° and stress distributions under three different settings: zero, one, and two spring partitions. A single chamber was pressurized to induce bending. (**B**) Effective bending angle versus applied pressure to the soft chamber, varied from zero to five spring partitions. (**C**) Maximum von Mises stresses in each model plotted against bending angle.

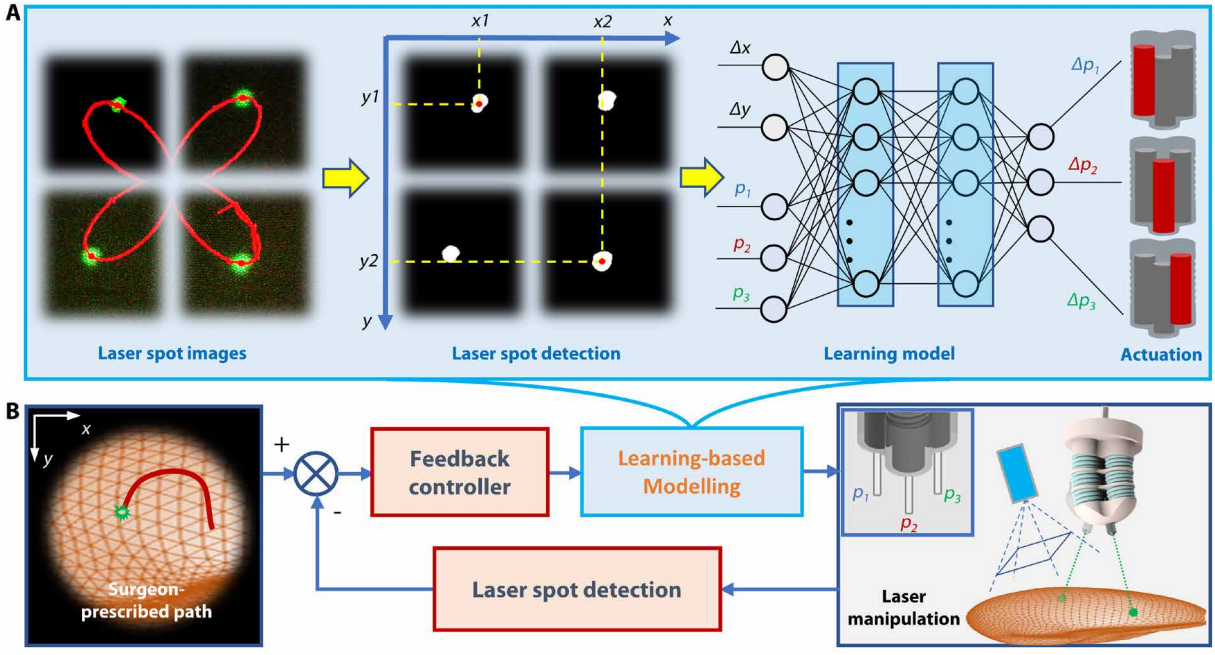

Fig. 8. Architecture of the proposed learning-based controller. (**A**) Overview of the learning-based model. The laser spot position in the camera view is varied by the laser manipulator. 2D displacements of the laser spot, along with the soft actuation states, act as inputs of a multilayer perceptron, which map to the actuation changes of each chamber. (**B**) The feedback control loop. With this learned inverse mapping, the proposed eye-to-hand visual servoing controller allows laser steering along paths prescribed in situ by the operator.

local stresses, thus enhancing robot response with minimized hysteresis while maintaining adequate robot durability. The distal laser manipulator actuation is effectively decoupled from the active bending section, allowing stable and repeatable kinematics and thus high-accuracy laser control. Integrated with an optical laser fiber, the robot enabled endoscopic laser delivery and operating in the oropharyngeal region with submillimeter accuracy (<~0.2 mm). A patient-specific dental guard was designed to create an open-jaw cavity for robot anchorage and access of auxiliary instruments such as a fiberscope. The entire robotic system passed MR compatibility testing with no EM artifacts, which allows full robot operation during imaging even at the MRI scanner isocenter.

The active bending section offered a 60° omnidirectional bending workspace for coarse navigation to the region of interest. The distal laser manipulator allowed fine laser beam pan-tilting (±26°) in a local target area, with a maximum scanning area of 15 mm by 15 mm at a 15-mm projection distance. Combined with a learning-based controller, accurate laser spot manipulation was achieved, with a mean tracking error < 200 μm in path after tasks. Preclinical trials have been conducted to evaluate the robot performance both with ex vivo swine tissue and a cadaver model. During ex vivo tissue testing, we investigated the use of anatomical T2 imaging and MR thermometry on monitoring laser ablation; our results indicated the potential for measuring laser ablation depth and temperature diffusion region. A cadaver trial was performed to validate the robot setup/anchorage, intra-op MRI guidance, and the visual servo-based laser beam manipulation in actual human anatomy. The robot achieved precise and automated path following of the laser spot along a trajectory defined in situ by the surgeon. During the ablation, MR thermometry was performed to measure the thermal diffusion process in the ablated lesion. The robot provided a stable platform during laser ablation due to the rigid anchorage of its base with the dental guard. In the current practice of treating oropharyngeal tumors, patients are placed under general anesthesia with muscle paralysis. With this in mind, our system is expected to maintain similar levels of motion stability as demonstrated in our cadaver testing. The outer cover capsulizing the distal laser manipulator also provides protection from contact with local anatomy.

With the flexible endoscopic approach, the proposed robotic system enabled direct exposure of the ablation laser to the target lesion, without the need for positioning patients with extreme neck extension to accommodate rigid laser micromanipulators. Moreover, by introducing MRI guidance, clinicians could have intuitive and precise feedback of the ablation process, which is critical for function preservation of surrounding structures. Temperature diffusion monitoring proved to be useful in laser surgery because thermal dose and accumulated tissue damage could be calculated accordingly. MR parameters sensitive to temperature, such as proton resonance frequency, were adjusted so that the MR susceptibility at high SNR could be used to measure small changes of temperature with <1°C accuracy. Combined with advanced MR sequences, even 3D resection margins can be evaluated intraoperatively to determine the completeness of laser excision/resection. This could protect critical healthy structures while eliminating the need for frozen section analysis, thus smoothing the surgical workflow and shortening operation time.

For future work, we plan to implement real-time MRI sequences customized for the laser ablation monitoring, optimizing for higher temporal resolution while maintaining sufficient imaging (spatial) resolution. Custom real-time sequences interleaving multislice anatomical and thermometry images bring the potential for greatly enhanced ablation monitoring and could enable automated laser ablation

control based on MRI feedback. We also aim to overlay in situ MRI on the fiberscope camera view, providing an augmented reality environment to further assist surgeons in evaluating the ablation process. A promising extension of this work is to couple optical coherence tomography (OCT) with the ablation setting by adopting the lens-pigtailed optical fiber as an OCT sampling arm, which can provide tissue depth images in micrometer-scale resolution. Alongside with the proposed laser steering mechanism, scanning paths/patterns could be performed to form 3D forward-viewing OCT images underlying the lesion. Visual servo of the laser spot projected on tissue would enable the operator to prescribe any preferred OCT scanning profile in situ in the endoscopic view, thus facilitating tissue/tumor characterization at the cellular scale, apart from using MRI.

MATERIALS AND METHODS

Oncologic management of HNCs requires local-regional control of disease, as well as preservation of speech and swallowing functions (*15*). There is often a dilemma between adequate tissue margin for clearance and functional destruction from over-resection. To enable agile delivery of laser energy to target regions, the robot should provide dexterous navigation through intraoral and oropharyngeal cavities, even down to the hypopharynx and larynx. The robotic scope should ensure safe contact with upper airway and also offer a stable platform for precise and local control of laser beam projection on oral and pharyngeal lesions.

Provided with intra-op MR anatomical and temperature images, tumor margins can be identified in situ, and the ablation/incision depth can be monitored in real time. This ensures that tumors/lesions are marked and resected with a margin of 5 to 10 mm beyond the tumor (*56*). To monitor minute physiological changes in the region of the lesion, zero image artifacts have to be ensured even during robot operation in close proximity to the region of interest. To this end, the robot should meet the rigorous requirement of zero EM interference, comprising no conductive, metallic, or magnetic components, i.e., the MR safety defined in the ASTM F2503 standard (*57*).

Design optimization of the soft manipulator

FEA was conducted to simulate the robot characteristics upon pressurization (Fig. 7A), thus facilitating the design optimization. The specific strain-stress relationship of the selected elastomer (i.e., AgilusClear30) was evaluated through a uniaxial tensile test and approximated by the Ogden model in the simulation. The robot structure was tessellated with the quadratic tetrahedron element (e.g., Abaqus C3D10H). Strain hardening/stiffening effects were considered such that the nonlinear stress-strain behavior can be simulated using specific methods, such as arc length.

Two model characteristics in terms of (i) bending angle and (ii) maximum von Mises stress were analyzed to evaluate the effect of partitions in the reinforced spring model. As shown in Fig. 7B, the effective bending angle decreases with more spring partitions, meaning that a greater pressure is required to overcome the additional model rigidity. This implies that the bending stiffness of soft manipulator is increased with spring partitions. Meanwhile, the maximum von Mises stress of the model increases with the partition number, as shown in Fig. 7C. The enhanced stiffness could improve the hysteresis and responsiveness of soft manipulator, thus allowing accurate laser beam control. However, high local stress would introduce model fracture and reduce the robot durability. Three are the optimized numbers of partitions, balancing the trade-off between high bending stiffness and local material rupture. Another concern is the twisting of the soft actuator caused by the extension of each spring structure. Our FEA indicates that the average twisting angle is negligible (<1°) and reduced with the spring partition number. Each partition connects the three individual chambers/spring coils, which causes them to share the twisting loading, ultimately simplifying the bending kinematics and improving robot controllability.

Mechanical response evaluation

Workspace

The maximum bending angles of the fabricated soft segments upon pressurization were measured using an EM tracking system (NDI Aurora). The laser manipulator can steer the laser lens to a maximum angle of ±26° (fig. S2A), which enables a scanning area of 15 mm by 15 mm at a 15-mm projection distance. As for the active bending section, our design offers an angular workspace of ±60°, which can be further enlarged by elongating the segment length or reducing the number of spring partitions.

Frequency response

The dynamics response of soft manipulator under hydraulic actuation was tested. The soft chamber was inflated/deflated through a hydraulic cylinder actuated by a servo motor. A 10-m-long hydraulic pipeline was used to meet the transmission requirements between MRI and control room. The positional output of the robot tip under periodic sinusoidal input from 0.1 to 5 Hz was captured by an EM tracking marker. Fourier analysis was conducted to evaluate the harmonic response. As shown in fig. S2B, the bandwidth was approximately 1 Hz, at which the magnitude response decreased −3 dB. This indicates that the changing frequency of positional command should be less than 1 Hz to prevent filtering by the soft robotic system. The bandwidth is intrinsically governed by the robot stiffness, which could be improved by fabricating the spring constraint with stiffer materials (e.g., polyether ether ketone). The phase lag was kept less than 35° within the bandwidth. The transmission latency or time delay from the computer signal to distal output was measured as 83 ms, on average, with the input frequency less than 1 Hz.

Durability

The reliability of soft chambers (e.g., material fatigue) should be maintained in a prescribed amount of usage, despite the intention to be a single-use device. As shown in fig. S2C, the soft manipulator was inflated (actuation step 2200) and deflated (actuation step 0) repeatedly 2000 times over a period of 1 hour. The robot remained functional, whereas the absolute bending angle decreased only 1.5°, which can be compensated for by a feedback controller or an online-updated learning model as discussed in the next section.

Hysteresis

We tested the hysteresis of soft manipulator by measuring its bending angle upon loading and unloading to the elastomer chambers. Two consecutive actuation cycles were performed. Figure S2D shows that the soft robot has a maximum hysteresis angle of 0.35°, which is negligible. This is attributed to the rigid SRCs that mechanically compensate for the hysteresis originating from the elastomeric material.

Learning-based controller

A visual servoing controller was implemented to achieve automatic targeting of the laser spot that could be projected along any trajectory that is prescribed in situ on the endoscopic view. The prerequisite is to form an adaptive kinematics model approximating the nonlinear

inverse mapping from image space to robot actuation space. Conventional kinematics methods require accurate characterization of robot structural parameters and actuation response, which is a well-known challenge for the intrinsic nonlinear hyperelastic property of elastomeric materials. In contrast, data-driven methods (*58*) such as machine learning approaches could accommodate modeling uncertainties from the actual operation data and eliminate the need for hand-eye calibration.

The presented learning-based controller is initialized by training a neural network (NN) with time-varying 2D laser spot displacements (Δx, Δy) and soft actuation status (p_i, $i = 1$, 2, and 3) as its input, and the corresponding actuation changes (Δp_i, $i = 1$, 2, and 3) as its output (Fig. 8A). The data were collected by commanding the laser manipulator to explore the workspace with a predefined scanning pattern (e.g., spiral). Relative movements rather than absolute positions of the laser spot were used to train a model so that it is robust to variation of viewing depth, which would scale the relative movements but completely shift the absolute positions. The actuation status represents the absolute inflation volumes (0 to 0.004 ml) of three soft chambers and determines the robot configuration. It was also incorporated as an input to facilitate spatially localizing the inverse kinematics problem, thereby ensuring the convexity of the solution set. This is driven by the insight that the differential inverse kinematics of a nonlinear system can be linearized locally.

The green laser spot with monochromatic color and high intensity was recognized by thresholding the captured red-green-blue images. Five thousand data samples were collected and divided randomly into training/validation/testing sets in the ratio of 80/10/10, respectively. A multilayer perceptron with two hidden layers and one output layer, using tan-sigmoid and linear transfer function, respectively, was used for learning. Levenberg-Marquardt backpropagation was used to train the network parameters. The sizes of the hidden layers were selected (20 nodes in each layer) to fulfill a high goodness of fit with the correlation coefficient > 0.99. The network was trained using the "fitnet" function in Matlab with Intel Core i7-8750H CPU @2.20 GHz. During each control loop, the desired laser spot movement as well as the actuation status will be inputted to the trained model. The trained NN model will always output a valid set of liquid volumes pumping in/out of the three soft chambers, which is inherently bounded by the training data. The trained NN model enables output prediction at high frequency (>100 Hz) for real-time robot control. Laser spot positions in camera view can be extracted online and fed back to close the control loop of soft actuation (Fig. 8B). Image acquisition and laser spot detection were implemented in a process written by C++, which was running in parallel with the main control loop. The feedback controller compensates for the tracking errors in real time (>20 Hz) and further improves the control accuracy. A feedback delay of ~30 ms was introduced by the camera image acquisition and processing, as well as communication with the main control loop. However, it is acceptable due to the limited bandwidth of soft actuation, resulting in a maximum laser steering speed of 2 mm/s. Note that an online updated controller can be also realized using nonparametric learning kernels, e.g., Gaussian process regression (*59*), to accommodate gradual change of robot characteristics.

SUPPLEMENTARY MATERIALS

robotics.sciencemag.org/cgi/content/full/6/57/eabg5575/DC1
Figs. S1 and S2
Movies S1 to S6

REFERENCES AND NOTES

1. L. Q. M. Chow, Head and neck cancer. *N. Engl. J. Med.* **382**, 60–72 (2020).
2. J. Attra, N. Kokot, in *Biomedical Optics in Otorhinolaryngology* (Springer, 2016), pp. 183–201.
3. G. Sankaranarayanan, R. R. Resapu, D. B. Jones, S. Schwaitzberg, S. De, Common uses and cited complications of energy in surgery. *Surg. Endosc.* **27**, 3056–3072 (2013).
4. C. Arens, Transoral treatment strategies for head and neck tumors. *GMS Curr. Top. Otorhinolaryngol. Head Neck Surg.* **11**, Doc05 (2012).
5. S. M. Zeitels, J. A. Burns, Oncologic efficacy of angiolytic KTP laser treatment of early glottic cancer. *Ann. Otol. Rhinol. Laryngol.* **123**, 840–846 (2014).
6. N. P. Parker, M. S. Weidenbecher, A. D. Friedman, B. A. Walker, D. G. Lott, KTP laser treatment of early glottic cancer: A multi-institutional retrospective study. *Ann. Otol. Rhinol. Laryngol.* **130**, 47–55 (2021).
7. M. Karaman, T. Gün, B. Temelkuran, E. Aynacı, C. Kaya, A. M. Tekin, Comparison of fiber delivered CO 2 laser and electrocautery in transoral robot assisted tongue base surgery. *Eur. Arch. Otorhinolaryngol.* **274**, 2273–2279 (2017).
8. M. K. Bhayani, F. C. Holsinger, S. Y. Lai, A shifting paradigm for patients with head and neck cancer: Transoral robotic surgery (TORS). *Oncology* **24**, 1010 (2010).
9. D. G. Grant, M. L. Hinni, J. R. Salassa, W. C. Perry, R. E. Hayden, J. D. Casler, Oropharyngeal cancer: A case for single modality treatment with transoral laser microsurgery. *Arch. Otolaryngol.* **135**, 1225–1230 (2009).
10. W. Steiner, O. Fierek, P. Ambrosch, C. P. Hommerich, M. Kron, Transoral laser microsurgery for squamous cell carcinoma of the base of the tongue. *Arch. Otolaryngol.* **129**, 36–43 (2003).
11. J. A. Burns, J. B. Kobler, J. T. Heaton, G. Lopez-Guerra, R. R. Anderson, S. M. Zeitels, Thermal damage during thulium laser dissection of laryngeal soft tissue is reduced with air cooling: Ex vivo calf model study. *Ann. Otol. Rhinol. Laryngol.* **116**, 853–857 (2007).
12. S. M. Zeitels, J. A. Burns, L. M. Akst, R. E. Hillman, M. S. Broadhurst, R. R. Anderson, Office-based and microlaryngeal applications of a fiber-based thulium laser. *Ann. Otol. Rhinol. Laryngol.* **115**, 891–896 (2006).
13. S. Ayari-Khalfallah, C. Fuchsmann, P. Froehlich, Thulium laser in airway diseases in children. *Curr. Opin. Otolaryngol. Head Neck Surg.* **16**, 55–59 (2008).
14. E. Passacantilli, M. Antonelli, A. D'Amico, C. P. Delfinis, G. Anichini, J. Lenzi, A. Santoro, Neurosurgical applications of the 2-μm thulium laser: Histological evaluation of meningiomas in comparison to bipolar forceps and an ultrasonic aspirator. *Photomed. Laser Surg.* **30**, 286–292 (2012).
15. K. M. Van Abel, E. J. Moore, M. L. Carlson, J. A. Davidson, J. J. Garcia, S. M. Olsen, K. D. Olsen, Transoral robotic surgery using the thulium: YAG laser: A prospective study. *Arch. Otolaryngol.* **138**, 158–166 (2012).
16. J. D. Richmon, Transoral palate-sparing nasopharyngectomy with the Flex® system: Preclinical study. *Laryngoscope* **125**, 318–322 (2015).
17. M. Benazzo, P. Canzi, A. Occhini, Transoral robotic surgery with laser for head and neck cancers: A feasibility study. *ORL* **74**, 124–128 (2012).
18. S. M. Olson, M. Hussaini, J. S. Lewis Jr., Frozen section analysis of margins for head and neck tumor resections: Reduction of sampling errors with a third histologic level. *Mod. Pathol.* **24**, 665–670 (2011).
19. H. Alsaffar, D. Goldstein, E. King, J. de Almeida, D. Brown, R. Gilbert, P. J. Gullane, O. Espin-Garcia, W. Xu, J. Irish, Correlation between clinical and MRI assessment of depth of invasion in oral tongue squamous cell carcinoma. *J. Otolaryngol. Head Neck Surg.* **45**, 61 (2016).
20. V. Rieke, K. Butts Pauly, MR thermometry. *J. Magn. Reson. Imag.* **27**, 376–390 (2008).
21. M. Marx, P. Ghanouni, K. Butts Pauly, Specialized volumetric thermometry for improved guidance of MRgFUS in brain. *Magn. Reson. Med.* **78**, 508–517 (2017).
22. M. Lepetit-Coiffé, H. Laumonier, O. Seror, B. Quesson, M.-B. Sesay, C. T. Moonen, N. Grenier, H. Trillaud, Real-time monitoring of radiofrequency ablation of liver tumors using thermal-dose calculation by MR temperature imaging: Initial results in nine patients, including follow-up. *Eur. Radiol.* **20**, 193–201 (2010).
23. D. Silva, M. Sharma, R. Juthani, A. Meola, G. H. Barnett, Magnetic resonance thermometry and laser interstitial thermal therapy for brain tumors. *Neurosurg. Clinics* **28**, 525–533 (2017).
24. R. J. McNichols, A. Gowda, M. Kangasniemi, J. A. Bankson, R. E. Price, J. D. Hazle, MR thermometry-based feedback control of laser interstitial thermal therapy at 980 nm. *Lasers Surg. Med.* **34**, 48–55 (2004).
25. Z. He, Z. Dong, G. Fang, J. D.-L. Ho, C.-L. Cheung, H.-C. Chang, C. C.-N. Chong, J. Y.-K. Chan, D. T. M. Chan, K.-W. Kwok, Design of a percutaneous MRI-guided needle robot with soft fluid-driven actuator. *IEEE Robot. Autom. Lett.* **5**, 2100–2107 (2020).
26. E. Franco, M. Ristic, M. Rea, W. M. W. Gedroyc, Robot-assistant for MRI-guided liver ablation: A pilot study. *Med. Phys.* **43**, 5347–5356 (2016).
27. Y. Chen, A. Squires, R. Seifabadi, S. Xu, H. K. Agarwal, M. Bernardo, P. A. Pinto, P. Choyke, B. Wood, Z. T. H. Tse, Robotic system for MRI-guided focal laser ablation in the prostate. *IEEE/ASME Trans. Mechatron.* **22**, 107–114 (2016).

28. R. Seifabadi, M. Li, S. Xu, Y. Chen, A. Squires, A. H. Negussie, I. Bakhutashvili, P. Choyke, I. B. Turkbey, Z. T. H. Tse, B. J. Wood, MRI robot for prostate focal laser ablation: An ex vivo study in human prostate. *J. Imag.* **4**, 140 (2018).
29. H. Su, W. Shang, G. Cole, G. Li, K. Harrington, A. Camilo, J. Tokuda, C. M. Tempany, N. Hata, G. S. Fischer, Piezoelectrically actuated robotic system for MRI-guided prostate percutaneous therapy. *IEEE/ASME Trans. Mechatron.* **20**, 1920–1932 (2014).
30. A. E. Sloan, M. S. Ahluwalia, J. Valerio-Pascua, S. Manjila, M. G. Torchia, S. E. Jones, J. L. Sunshine, M. Phillips, M. A. Griswold, M. Clampitt, C. Brewer, J. Jochum, M. V. McGraw, D. Diorio, G. Ditz, G. H. Barnett, Results of the NeuroBlate System first-in-humans Phase I clinical trial for recurrent glioblastoma. *J. Neurosurg.* **118**, 1202–1219 (2013).
31. Z. Guo, Z. Dong, K.-H. Lee, C. L. Cheung, H.-C. Fu, J. D. Ho, H. He, W.-S. Poon, D. T.-M. Chan, K.-W. Kwok, Compact design of a hydraulic driving robot for intraoperative MRI-guided bilateral stereotactic neurosurgery. *IEEE Robot. Autom. Lett.* **3**, 2515–2522 (2018).
32. H. Su, G. Li, D. C. Rucker, R. J. Webster III, G. S. Fischer, A concentric tube continuum robot with piezoelectric actuation for MRI-guided closed-loop targeting. *Ann. Biomed. Eng.* **44**, 2863–2873 (2016).
33. D. B. Comber, E. B. Pitt, H. B. Gilbert, M. W. Powelson, E. Matijevich, J. S. Neimat, R. J. Webster III, E. J. Barth, Optimization of curvilinear needle trajectories for transforamenal hippocampotomy. *Operative Neurosurg.* **13**, 15–22 (2017).
34. D. Kundrat, R. Graesslin, A. Schoob, D. Friedrich, M. Scheithauer, T. Hoffmann, T. Ortmaier, L. A. Kahrs, P. Schuler, Preclinical performance evaluation of a robotic endoscope for non-contact laser surgery. *Ann. Biomed. Eng.* **49**, 585–600 (2021).
35. M. Zhao, T. J. O. Vrielink, A. A. Kogkas, M. S. Runciman, D. S. Elson, G. P. Mylonas, LaryngoTORS: A novel cable-driven parallel robotic system for transoral laser phonosurgery. *IEEE Robot. Autom. Lett.* **5**, 1516–1523 (2020).
36. P. A. York, R. Peña, D. Kent, R. J. Wood, Microrobotic laser steering for minimally invasive surgery. *Sci. Robot.* **6**, eabd5476 (2021).
37. R. Renevier, B. Tamadazte, K. Rabenorosoa, L. Tavernier, N. Andreff, Endoscopic laser surgery: Design, modeling, and control. *IEEE/ASME Trans. Mechatron.* **22**, 99–106 (2016).
38. E. Tumino, R. Sacco, M. Bertini, M. Bertoni, G. Parisi, A. Capria, Endotics system vs colonoscopy for the detection of polyps. *World J. Gastroenterol.* **16**, 5452–5456 (2010).
39. F. Cosentino, E. Tumino, G. R. Passoni, E. Morandi, A. Capria, Functional evaluation of the endotics system, a new disposable self-propelled robotic colonoscope: In vitro tests and clinical trial. *Int. J. Artif. Organs* **32**, 517–527 (2009).
40. M. Cianchetti, T. Ranzani, G. Gerboni, T. Nanayakkara, K. Althoefer, P. Dasgupta, A. Menciassi, Soft robotics technologies to address shortcomings in today's minimally invasive surgery: The STIFF-FLOP approach. *Soft Robot.* **1**, 122–131 (2014).
41. Z. Dong, Z. Guo, K.-H. Lee, G. Fang, W. L. Tang, H.-C. Chang, D. T. M. Chan, K.-W. Kwok, High-performance continuous hydraulic motor for MR safe robotic teleoperation. *IEEE Robot. Autom. Lett.* **4**, 1964–1971 (2019).
42. D. B. Comber, J. E. Slightam, V. R. Gervasi, J. S. Neimat, E. J. Barth, Design, additive manufacture, and control of a pneumatic MR-compatible needle driver. *IEEE Trans. Robot.* **32**, 138–149 (2016).
43. L. Fichera, *Cognitive Supervision for Robot-Assisted Minimally Invasive Laser Surgery* (Springer Nature, 2016).
44. R. V. Martinez, C. R. Fish, X. Chen, G. M. Whitesides, Elastomeric origami: Programmable paper-elastomer composites as pneumatic actuators. *Adv. Funct. Mater.* **22**, 1376–1384 (2012).
45. Z. Wang, P. Polygerinos, J. T. B. Overvelde, K. C. Galloway, K. Bertoldi, C. J. Walsh, Interaction forces of soft fiber reinforced bending actuators. *IEEE/ASME Trans. Mechatron.* **22**, 717–727 (2017).
46. C.-L. Cheung, J. D.-L. Ho, V. Vardhanabhuti, H.-C. Chang, K.-W. Kwok, Design and fabrication of wireless multilayer tracking mrker for intraoperative MRI-guided interventions. *IEEE/ASME Trans. Mechatron.* **25**, 1016–1025 (2020).
47. N. Punhani, G. R. Dongarwar, H. Mahajan, M. J. Daniel, K. Chalapathi, A. S. Nayyar, Tumor size and its relation to cervical lymph node metastasis and its significance as a prognostic indicator for oral squamous cell carcinomas. *Clin. Cancer Investig. J.* **6**, 153–166 (2017).
48. N. E. M. Association, Determination of signal-to-noise ratio (SNR) in diagnostic magnetic resonance imaging, in *NEMA Standards Publication MS 1–2001* (2001).
49. K. Chinzei, K. Miller, MRI guided surgical robot, in *Australian Conference on Robotics and Automation* (2001), pp. 50–55.
50. ASTM, Standard test method for evaluation of MR image artifacts from passive implants, in *ASTM F2119* (2001).
51. Z. Zhang, T. Michaelis, J. Frahm, Towards MRI temperature mapping in real time—The proton resonance frequency method with undersampled radial MRI and nonlinear inverse reconstruction. *Quant. Imaging Med. Surg.* **7**, 251–258 (2017).
52. S. Toupin, P. Bour, M. Lepetit-Coiffé, V. Ozenne, B. D. de Senneville, R. Schneider, A. Vaussy, A. Chaumeil, H. Cochet, F. Sacher, P. Jaïs, B. Quesson, Feasibility of real-time MR thermal dose mapping for predicting radiofrequency ablation outcome in the myocardium in vivo. *J. Cardiovasc. Magn. Reson.* **19**, 14 (2017).
53. A. L. Gough-Palmer, W. M. W. Gedroyc, Laser ablation of hepatocellular carcinoma-A review. *World J. Gastroenterol* **14**, 7170–7174 (2008).
54. M. O. Köhler, C. Mougenot, B. Quesson, J. Enholm, B. Le Bail, C. Laurent, C. T. W. Moonen, G. J. Ehnholm, Volumetric HIFU ablation under 3D guidance of rapid MRI thermometry. *Med. Phys.* **36**, 3521–3535 (2009).
55. N. J. Mickevicius, E. S. Paulson, Simultaneous orthogonal plane imaging. *Magn. Reson. Med.* **78**, 1700–1710 (2017).
56. W. I. Wei, W. K. Ho, Transoral robotic resection of recurrent nasopharyngeal carcinoma. *Laryngoscope* **120**, 2011–2014 (2010).
57. ASTM, Standard practice for marking medical devices and other items for safety in the magnetic resonance environment, in *ASTM F2503-13* (2013).
58. K.-H. Lee, D. K. C. Fu, M. C. W. Leong, M. Chow, H.-C. Fu, K. Althoefer, K. Y. Sze, C.-K. Yeung, K.-W. Kwok, Nonparametric online learning control for soft continuum robot: An enabling technique for effective endoscopic navigation. *Soft Robot.* **4**, 324–337 (2017).
59. G. Fang, X. Wang, K. Wang, K.-H. Lee, J. D. Ho, H.-C. Fu, D. K. C. Fu, K.-W. Kwok, Vision-based online learning kinematic control for soft robots using local gaussian process regression. *IEEE Robot. Autom. Lett.* **4**, 1194–1201 (2019).
60. B. Banko, V. Djukic, J. Milovanovic, G. Lilic, M. Kratovac-Dunjic, R. Milenkovic, R. Maksimovic, Preoperative staging of laryngeal carcinoma: Comparison of CT and MRI with histopathology, in *European Congress of Radiology 2013* (2013).
61. D.-M. Denk, R. Schöfl, in *Radiology of the Pharynx and the Esophagus* (Springer, 2004), pp. 167–181.

Acknowledgments: We thank X. M. Wang, C. L. Cheung, W. L. Tang, J. Dai, and R. Y. Xie for assistance with the experiments. **Funding:** This work was supported by the Research Grants Council (RGC) of Hong Kong (17202317, 17206818, 17205919, and T42-409/18-R) and the Innovation and Technology Commission (ITC) (nos. UIM/353 and ITS/435/18FX). **Author contributions:** J.Y.-K.C. and K.-W.K. initiated and conceptualized the project. T.C.N. investigated the demand for non–contact-based laser therapy. M.C.K.C., G.F., J.D.L.H., and K.-W.K. designed and fabricated the robot system. T.C.N. and J.K.H.T. assisted with the dental guard design. G.F. designed and implemented robot control algorithms. K.W. conducted the FEA. M.C.K.C., G.F., Z.H., and J.D.L.H. designed and performed experimentation. D.T.-M.C., J.Y.-K.C., P.-L.C., F.C.H., and Y.-H.L. provided clinical input, supporting the cadaver trial. H.-C.C. implemented the MR thermometry and designed the MRI settings. K.-W.K., G.F., and J.D.L.H. prepared the manuscript and figures. All authors reviewed and edited the manuscript. **Competing interests:** J.Y.-K.C., J.D.L.H., M.C.K.C., and K.-W.K. have a provisional patent application on the design of MR-safe soft laser manipulators. J.Y.-K.C., H.C.C., G.F., J.D.L.H., M.C.K.C., and K.-W.K. have a provisional patent application on visual servoing control of soft laser manipulators. The other authors declare that they have no competing interests. **Data and materials availability:** All data needed to support the conclusions of this manuscript are included in the main text or the Supplementary Materials.

Submitted 15 January 2021
Accepted 27 July 2021
Published 18 August 2021
10.1126/scirobotics.abg5575

Citation: G. Fang, M. C. Chow, J. D.-L. Ho, Z. He, K. Wang, T. Ng, J. K. Tsoi, P.-L. Chan, H.-C. Chang, D. T.-M. Chan, Y.-h. Liu, F. C. Holsinger, J. Y.-K. Chan, K.-W. Kwok, Soft robotic manipulator for intraoperative MRI-guided transoral laser microsurgery. *Sci. Robot.* **6**, eabg5575 (2021).

Science Robotics

Soft robotic manipulator for intraoperative MRI-guided transoral laser microsurgery

Ge FangMarco C. K. ChowJustin D. L. HoZhuoliang HeKui WangT. C. NgJames K. H. TsoiPo-Ling ChanHing-Chiu ChangDanny Tat-Ming ChanYun-hui LiuF. Christopher HolsingerJason Ying-Kuen ChanKa-Wai Kwok

Sci. Robot., 6 (57), eabg5575.

Science Robotics (ISSN) is published by the American Association for the Advancement of Science. 1200 New York Avenue NW, Washington, DC 20005. The title *Science Robotics* is a registered trademark of AAAS.